Artificial nucleation sites with stable SEI for Li metal anodes by aggressive Al pulverization

Feihong Ren, Zhendong Li, Yun Zhu, Patrice Huguet, Stefano Deabate, Deyu Wang, Zhe Peng

Artificial Nucleation Sites with Stable SEI for Li metal anodes by Aggressive Al Pulverization

Feihong Ren,[a] Zhendong Li,[b] Yun Zhu,[b] Patrice Huguet,[a] Stefano Deabate,[a,*] Deyu Wang,[b,*] and Zhe Peng[b,*]

a. IEM (Institut Européen des Membranes), UMR 5635 (UM-ENSCM-CNRS), Université de Montpellier, Place E. Bataillon, F-34095, Montpellier, France.

b. Ningbo Institute of Materials Technology and Engineering, Chinese Academy of Sciences, Ningbo 315201, China.

Corresponding Author

*E-mail: (S. D.) stefano.deabate@univ-montp2.fr; (D. W.) wangdy@nimte.ac.cn; (Z. P.) pengzhe@nimte.ac.cn

Abstract

Uneven nucleation and fragile solid electrolyte interphase (SEI) restrict the practical application of lithium (Li) metal anode. A versatile strategy to simultaneously overcome these two drawbacks is critical for Li metal batteries (LMBs). Herein we propose an "aggressive aluminum (Al) pulverization" strategy to form abundant artificial nucleation sites and robust SEI films adjacently, leading to homogeneous Li deposition/stripping and high Li Coulombic efficiency. A core-shell structure with Al core and alumina-silica (Al_2O_3-SiO_2) shell, Al@Al_2O_3-SiO_2 (AAS), could be easily synthesized, by modulating the chemical diffusion of silicon (Si) element towards Si-Al alloy surface. The active SiO_2 sites not only contribute to form the robust SEI layer, but also facility the lithiation of the AAS, accelerating the conversion of reversible Li-Al alloy into inert Li_3Al_2 phase. The as-generated AAS with Li_3Al_2 and $Li_{12}Si_7$ phases possess negligible Li nucleation over-potential (~0.7 mV), serving as an optimal structure for dendrite-free Li plating/stripping with a prolonged life-span of 6 times longer than that of the unprotected counterpart in carbonate electrolytes.

Graphical Abstract

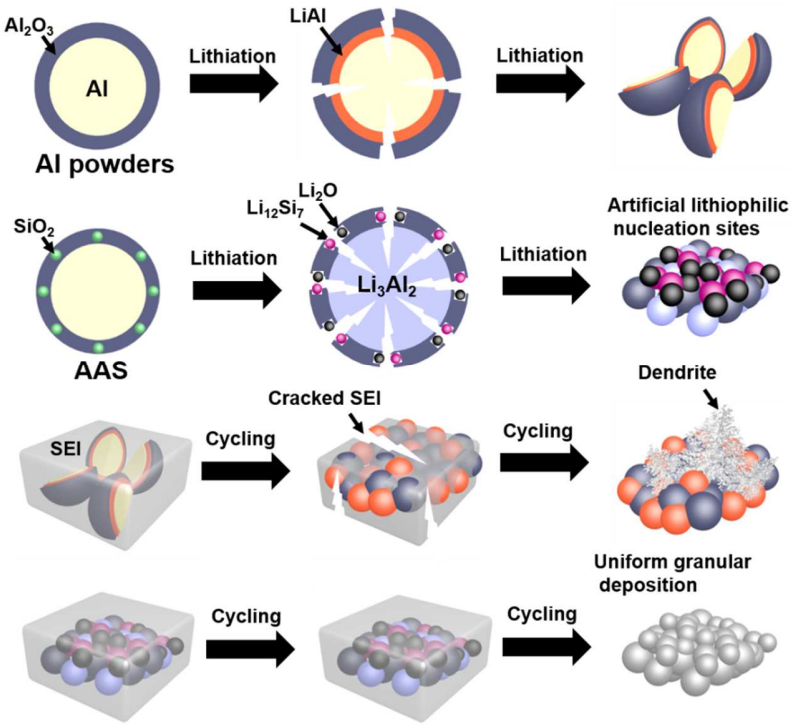

KEYWORDS: Lithium metal anode; Al pulverization; Li-Al alloy; Si chemical diffusion; solid electrolyte interphase.

1. Introduction

A great motivation of developing high-energy-density battery systems is derived from the gap between the upper energy density of the state-of-the-art lithium (Li) ion batteries (LIBs) and the ever-growing demand of portable electronic products, electric automobiles, and large-scale grid implementations [1]. Owing to the ultrahigh theoretical specific capacity (3860 mAh g^{-1}) and the lowest electrode potential (-3.04 V vs. standard hydrogen electrode) of Li metal anode [2,3], pairing Li metal anodes with high capacity cathodes (e.g., $LiNi_xCo_yMn_{1-x-y}O_2$, $xLi_2MnO_3 \cdot (1-x)LiMO_2$, S, O_2 and so on) is considered as a promising route to achieve next-generation high-energy-density Li metal batteries (LMBs) [4,5]. However, heterogeneous Li plating/stripping and fragile/resistive solid electrolyte interphase (SEI) layers lead to dendritic Li (e.g. mossy-like, needle-like) growth, fast capacity fading and eventual thermal runaway of LMBs, especially in carbonates electrolytes possessing wide voltage windows that are required for high-voltage LMBs [6-8].

To solve these problems, multiple strategies have been devoted, including optimizing electrolyte formulation to improve SEI layer quality [9-11], utilizing 3D hosts to accommodate Li deposition [12-14], and coating artificial protective layers [15-20]. Besides, initial Li nucleation has an essential influence on subsequent Li deposition morphology and overall electrochemical performance of Li metal anode [21-23]. Recently, Li-M alloy (M= Al, Si, Sn, etc.) has been proved helpful to realize dendrite-free Li metal anodes by guiding uniform Li nucleation, based on the alloying/dealloying processes of Li-M [24,25]. However, keeping the active Li-M alloy

with reversible alloying/dealloying processes seems to be a prerequisite for these structures, which is quite questionable for long-term cycling.

In this work, we demonstrate that the reversible alloying/dealloying processes of Li-Al are not necessary for achieving uniform Li nucleation. In contrast, converting the reversible Li-Al alloy into inert Li_3Al_2 granules through an "aggressive Al pulverization" strategy could serve as prominent artificial nucleation sites, outperforming that based on reversible alloying/dealloying processes of Li-Al alloy (Fig. 1a). Using Si-Al alloy micro-spheres as precursors, we modulated the chemical diffusion of Si element towards the surface of Si-Al alloy to synthesis a core-shell structure with Al core and alumina-silica (Al_2O_3-SiO_2) shell, Al@Al_2O_3-SiO_2 (AAS). The active SiO_2 sites not only contribute to form a robust Li_2O-rich SEI layer, but also facility the lithiation of the AAS, accelerating the conversion of reversible Li-Al alloy into inert Li_3Al_2 phase. Due to the complete pulverization of the AAS, no evident volume change was observed during subsequent cycling, while the as-generated AAS with Li_3Al_2 and $Li_{12}Si_7$ phases possesses negligible Li nucleation over-potential (~0.7 mV), resulting in stable SEI layer and uniform granular Li deposition (Fig. 1b). Meanwhile for conventional Al powders, a native Al_2O_3 surface layer inevitably exists, impeding fast lithiation due to its high chemical stability and insulating nature [26-28], and leading to gradual pulverization of the Al powders during repeated alloying/dealloying processes with large volume change and SEI layer breaks (Fig. 1a and Fig. 1b). Using the optimal AAS structure, dendrite-free Li plating/stripping was achieved with a prolonged life-span of 6 times longer than that of the unprotected counterpart in carbonate electrolytes. Furthermore, the AAS structure was successively applied in Li ‖ $LiFePO_4$ full cell, which could remain a highly stable cycling over 645 cycles with a capacity retention of 90.5%,

outperforming those using bare Li or Al powders protected Li. Hence, this method provides a novel approach of regulating Li nucleation for long-term cycling of stable LMBs with dendrite-free features.

2. Results and Discussion

The precursor of the AAS is Si-Al alloy micro-spheres consisted of Al backbone and uniformly dispersed Si, with a native Al_2O_3 layer formed on the surface (25 ℃, Fig. S1a). The disproportion of Si-Al elements in their hypoeutectic alloy could be achieved by modulating the chemical diffusion of Si element at different temperatures (Fig. S1b) [29]. The gradual diffusion of Si element from the inner space towards the surface of the Si-Al alloy micro-spheres is realized via a facile sintering method by heating the commercial Si-Al alloy powder (Si: 7.027%, Al: 92.973% in atomic ratio; Si: 7.293%, Al: 92.707% in mass ratio) on the temperature range between 25 and 1000 ℃, as demonstrated by their cross-sectional FIB-SEM images with EDS mapping (Fig. S1a). Finally, the AAS was obtained by sintering the Si-Al alloy at 1000 ℃ in air condition (Fig. 1c). In addition to the pre-existing Al_2O_3, SiO_2 was also formed on the outer layer of the AAS due to the oxidation of the diffused Si. As shown by the X-ray diffraction (XRD) patterns, the components of Al_2O_3, Al and SiO_2 are separately observed for the AAS, while the conventional Al powders only exhibit the dominant peaks of Al and weak signals of the native Al_2O_3 surface layer (Fig. 1d).

Interestingly, X-ray photoelectron spectroscopy (XPS) analysis showed different surface chemistry for the AAS and Al powders after the lithiation to 0 V vs. Li/Li^+ (Fig. 1e). Besides the major peak of Al_2O_3 (74.0 eV) on the Al 2p spectra for both the AAS and Al powders, the presence of Li_3Al_2 (71.2 eV) was observed on the AAS, while LiAl (71.7 eV) was observed on the Al powders. High-resolution transmission electron microscopy (HRTEM) images and corresponding fast Fourier transform (FFT) patterns of the lithiated AAS and Al powders are shown in Fig. 1f and Fig. 1g. Some nanoparticles with lattice fringes of Li_2O (200), Li_3Al_2 (016), $Li_{12}Si_7$ (683) and Al_2O_3 (116) are observed on the lithiated AAS (Fig. 1f), while the lithiated Al powders exhibit rather large bulk phase with lattice fringes of Al (220), LiAl (511) and Al_2O_3 (202) (Fig. 1g). The presence of Al (220) lattice fringe in the lithiated Al powders indicates the unreacted Al in its bulk phase. Based on the surface analysis of the lithiated AAS, the following electrochemical reaction equations could be presumed:

$$SiO_2+4Li^+ +4e^- \rightarrow 2Li_2O+Si \qquad (1)$$

$$7Si+12Li^+ +12e^- \rightarrow Li_{12}Si_7 \qquad (2)$$

Fig. 2a shows the first discharge curves including the lithiation of the AAS and Al powders (reduction to 0 V vs. Li/Li^+, stage ①) and subsequent Li plating of 1 mAh cm^{-2} (stage ②).

During the stage ①, the lithiation over-potential of Li-Al alloy for the AAS is ~116.8 mV, which is lower than that of the Al powders (~144.8 mV), indicating the facilitated Li^+ transfer through the solid/electrolyte interface of the AAS. The morphologies of the AAS and Al powders before/after lithiation are shown in Fig. 2b-2e. Before lithiation, the AAS and Al powders have similar micro-spherical shapes (Fig. 2b and 2c), whose frequency distributions of particle size both focused at 20 μm (Fig. S2). The initial AAS particles have a low Brunauer-Emmett-Teller (BET) surface area of 1.2769 $m^2 g^{-1}$ (Fig. S3a), with the presence of nanopores that could facility the lithiation process (Fig. S3b). In contrast, the Al powder possessed an abnormal adsorption-desorption curve due to the inaccessibility of nitrogen infiltration (Fig. S3c), indicating a very compact structure of the Al powders that leads to the impeded lithiation as shown in Fig. 2a. After lithiation, a deeply pulverized morphology was observed for the AAS (Fig. 2e), while granular morphology was still observed for the Al powders (Fig. 2d), indicating the pulverization of the Al powders is less aggressive than that of the AAS. Consistently, the specific capacity of lithiation for the AAS is 1326.1 mAh g^{-1} (Fig. 2a), close to the theoretical value for the conversion of Al into Li_3Al_2 (1410 mAh g^{-1}). Meanwhile the specific capacity of lithiation for the Al powders is only 693 mAh g^{-1} (Fig. 2a), which is even lower than that for the conversion of Al into LiAl (993 mAh g^{-1}), indicating the impeded lithiation due to the insulating Al_2O_3 outer layer.

In this work, 1 M $LiPF_6$/carbonate electrolyte (1 M $LiPF_6$ in EC:DEC (1:1, v/v) with vol. 5% FEC) was used as the control electrolyte to assess the ability of the AAS for Li protection, due to the wide voltage window of the carbonate electrolyte for high-voltage LMBs. As shown in Fig. S4, the element mapping show uniform distributions of C, O and F on the lithiated AAS. XPS

analysis with Ar^+ etching was performed to study the detailed surface chemistry of SEI layers on the AAS or Al powders after 10 cycles. As shown in Fig. 2f, the signals of Li_xPF_y, $Li_xPO_yF_z$ and LiF always exist on the surface of the Al powders, while LiF seems to be the only F-based component on the AAS up to an etching depth of 272 nm. The content of LiF is mainly generated from the reductive decomposition of $LiPF_6$ and FEC, while Li_xPF_y and $Li_xPO_yF_z$ are derived from the intermediate decomposition of $LiPF_6$ [30]. The radical reductions of $LiPF_6$ and FEC into LiF on the AAS are probably due to the facilitated charge transfer on the more active SiO_2-based native layer, while the LiF has long been demonstrated as a critical SEI component for stable Li plating/stripping [31,32]. Fig. 2g shows O 1s spectra at different depths of the surface on the AAS and Al powders, whereas a critical difference is the persistent presence of Al_2O_3 on the Al powders that results in the insulating layer impeding the lithiation of the Al powders. For the C 1s spectra (Fig. S5), the ratio of inorganic carbonates (CO_3^{2-}) to organic carbon groups on the AAS was lower than that on the Al powders, indicating higher content of Li_2CO_3 included in the SEI layer on the Al powders, which would enlarge the interfacial resistance because of its low electronic and ionic conductivity [33]. Based on the material characterizations and electrochemical behaviors of the lithiated AAS and Al powders, it is expected that the lithiated AAS could maintain a relatively stable structure during subsequent cycling, leading to stabilized SEI layer and high efficient Li plating/stripping.

In general, the solubility of Li in copper (Cu) is negligible [34], leading to the lithiophobic nature and large Li nucleation over-potential (> 100 mV) of Cu current collector during Li plating (stage ②, Fig. 2a). In contrast, the high solubility of Li in Al often leads to low Li nucleation over-potential. In the present case, the Li nucleation over-potentials on the AAS and Al powders

are ~0.7 and 3.7 mV, respectively (stage ②, Fig. 2a). The even lower Li nucleation over-potential on the AAS than that on the Al powders could be due to the Li_3Al_2 and $Li_{12}Si_7$ imbedded SEI layer on the AAS, while the surface layer of the Al powders is mainly consisted of Al_2O_3. The beneficial effect of $Li_{12}Si_7$ is consistent to the lithiophilic nature of Si-based surface layer as recently reported [35].

Based on the ultralow Li nucleation over-potential, uniform Li deposition is expected on the AAS. To investigate the latter, Li plating/stripping was applied to Cu foil, Al powders and AAS in the $LiPF_6$/carbonate electrolyte, at a current density of 0.5 mA cm^{-2} for a fixed areal capacity of 1 mAh cm^{-2}. The as-obtained morphologies were studied through scanning electron microscopy (SEM, Fig. 3). For the AAS, uniform and granular Li depositions were observed at different cycles (1^{st}, 10^{th}, 20^{th} and 50th cycles, Fig. 3i-3l), while the crack-free surfaces indicate the highly robust SEI layers formed on the aggressively pulverized AAS with low volume change. In contrast, interlaced cracks were gradually formed on bare Cu electrode with the cycling proceeding (Fig. 3a-3d), resulting from the poor SEI layer and uneven Li plating/stripping on the lithiophobic Cu substrate. As expected, due to the gradual pulverization, large volume changes were observed on the Al powders upon cycling (Fig. 3e-3h), leading to seriously cracked and heterogeneous SEI layers and side reactions. The Li plating morphology for a practical capacity of 5 mAh cm^{-2} was also studied at a scale of hundreds of microns, using an optical sealed cell coupled with a confocal laser scanning microscope. As shown in Fig. S6a, obvious surface roughness with tremendous needle-like structures was observed on the bare Li foil, showing the serious surface heterogeneity engendered by the dendrite growth. In contrast, smooth surface was maintained on the surface AAS even for the high capacity of 5 mAh cm^{-2}

(Fig. S6b), demonstrating the uniform Li deposition enabled by the lithiophilic sites and robust SEI layer formed on the AAS structure.

To further illustrate the effect of the aggressively pulverized AAS on Li metal protection, electrochemical impedance spectroscopy (EIS) spectra were recorded at the 5^{th}, 10^{th}, 15^{th} and 20^{th} cycles. As shown in Fig. 4a, the charge transfer resistance (R_{ct}) of the Al powders increases rapidly from ~33 to 122 Ω, indicating the largely accumulated resistive side products caused by the unstable interface between the electrode and electrolyte. In contrast, the cell using the AAS exhibits much smaller R_{ct} ranged on 20-40 Ω from the 5^{th} to 20^{th} cycles, demonstrating the much stabilized electrode/electrolyte interfaces with uniform Li plating/stripping and robust SEI layer.

Large volume expansion and repeated SEI cracks are the most considered failure causes of Li metal anode. However, another critical issue involving parasite incidences of LMBs is the gas generation at the Li anode surface due to the side reactions between the highly reactive Li and electrolyte. This issue was observed by in-situ μ-Raman measurements carried out near the investigated substrates during Li plating (Fig. 4b). As shown in Fig. 4c and Fig. 4d, at the beginning of Li plating, strong Raman bands at 710-760 cm^{-1} corresponding to the vibration of P-F symmetric stretch in PF_6^- anions are observed, while the bands at 715, 730 and 742 cm^{-1} mainly arise from free PF_6^-, Li^+-PF_6^- pair and $(Li^+)_n$-PF_6^- aggregate ($n \geqslant 2$) respectively [36,37]. Another group of Raman bands ranged on 850-940 cm^{-1} belong to the free/bonded organic solvents (EC, FEC, DEC), whereas the band centered at 867 cm^{-1} is related to free organic solvents, and the two bands centered at 895 and 905 cm^{-1} should arise from Li^+-solvent pairs [36,37]. Upon cycling, stable voltage profile and Raman spectra were maintained for the AAS,

indicating uniform Li plating process occurring on the lithiated AAS substrate (Fig. 4c). However, in the case of Li plating on the lithiated Al powders, large voltage fluctuations appeared with the cycling proceeding, and the signals of the related Raman spectra were seriously weakened (Fig. 4d). Since it is hard to ascribe the simultaneous weaknesses of the entire Raman bands to any possible side reactions, this sudden phenomenon is rather caused by a physical process, i.e. the gas generation.

Using the same cell as employed for in-situ Raman measurements, the optical images of 5 mAh cm^{-2} Li plating on the lithiated AAS and Al powders were recorded (Fig. 4e and Fig. 4f). Granular Li deposits with metallic luster were homogeneously dispersed on the lithiated AAS (Fig. 4e), consistent to the morphology observed with SEM (Fig. 3i-3l). In contrast, large dendritic deposition piercing the separator was observed on the lithiated Al powders, whereas tremendous gas bubbles were also noticed (Fig. 4f), which are probably the main cause affecting the laser scattering so as the signal weakness of Raman bands in Fig. 4d. Thus, based on the in-situ Raman measurements and optimal observations, it demonstrates the important role of an efficient protective structure for stable and uniform Li deposition, not only inhibiting the uncontrolled volume expansion and side reactions, but also limiting the undesired gas generation that could further cause a sophisticated battery management.

The improved interfacial stability of the AAS protected Li metal anode was also demonstrated using symmetrical cells, whereas the AAS was coated on the two sides of a Celgard separator to protect Li metal in the symmetric cells. A rate capability test was carried out prior to the long-

term cycling, by cycling the symmetrical cells at 0.5, 1, 2, 3, 4, and 5 mA cm^{-2} for a fixed areal capacity of 1 mAh cm^{-2} (Fig. 5a). During this dynamic test, much higher polarization was achieved for the cell using bare separator (Fig. 5b), implying the sluggish charge transfer at the interface of bare Li/electrolyte. The much reduced polarization for the cell using the AAS coated separator should arise from the lithiophilic Li_3Al_2 and $Li_{12}Si_7$ imbedded SEI layer. As shown in Fig. 5c, a large portion of 71.4% of the overall polarization is decreased sharply by using the AAS coated separator on the current density range of 0.5-5 mA cm^{-2}, reflecting a good ability for governing high-powder LMBs. Posterior to the rate capability test, the symmetric cell using the AAS coated separator provides a long-term and stable polarization of ~30 mV over 1000 h, whereas large voltage bumps inducing a drastic polarization up to 1000 mV were achieved at 270 h for the cell using bare separator, due to a seriously deteriorated interphase between Li anodes and electrolyte. As well, the AAS protected Li anode still kept a relatively smooth surface after a long cycling of 1000 h (digital photo shown in Fig. 5a), while a deep dark zone at the center of the unprotected Li anode appeared after the short cycling of 270 h. The latter indicates a heterogeneous distribution of Li^+ flux that accelerates the side reactions on the unprotected Li anode, while the AAS coating not only reduces the Li plating/stripping over-potentials, but also uniformizes the Li^+ flux and deposition morphology for highly stable Li anodes.

The Coulombic efficiency (CE) of Li plating/stripping was also assessed on the AAS. As expected, for the Si-Al alloy powders sintered at different temperatures as shown in Fig. 1c and Fig. S1a, the best CE was achieved for the Si-Al alloy powders sintered at 1000 ℃ (AAS, Fig. S7), demonstrating the critical role of SiO_2 as a surface component rather than a bulk phase in

the Si-Al alloy, which could further induce the formation of highly lithiophilic SEI layer as well as aggressively pulverized structure with Li_3Al_2 and $Li_{12}Si_7$ phases. The CE achieved on the AAS not only outperformed those of the Si-Al alloy powders sintered at lower temperatures than 1000 ℃, but also outperformed those on bare Cu and Al powders. The 1st CEs are 94.6%, 61.6% and 70.0% for bare Cu, Al powders and AAS, respectively. The lower CEs of Al powders and AAS than that of bare Cu are due to the higher specific surface areas of the artificial structures causing higher Li consumption to form SEI layers, which is a general concern for the use of artificial protective structures in LMBs, i.e. the need of pre-lithiation technique. Besides, the higher 1st CE of AAS than that of Al powders demonstrate the fully pulverized and lithiated state of AAS, resulting in less Li loss that is consumed in gradual alloying/dealloying processes of Al powders. This feature could also be illustrated by the 1st discharge-charge curves (Fig. S8), whereas evident dealloying curve is observed in the case of Al powders, while similar shapes are observed between the curves of AAS and bare Cu. As shown in Fig. 6a, the CE could be stably maintained at ~97% on the AAS electrodes over 300 cycles, which is 6 times more than that on Cu foil (with an average CE of ~87%) or Al powders (with an average CE of ~91%) in carbonate electrolytes. As illustrated by the discharge-charge curves at the 50th cycle (Fig. 6b), Li plating/stripping on Cu foil or Al powders show significantly larger polarizations than that for the AAS, due to the accumulation of resistive side products on the formers.

It should be mentioned that the Al_2O_3-SiO_2 shell formed on the AAS through the chemical diffusion of Si element is unique to generate the highly protective structure. As comparison, Li CE was also assessed on a simple physical mixture of SiO_2/Al_2O_3 powders at the same atomic ratio (Si: 7.027%, Al: 92.973%) as that in the Si-Al alloy (Fig. S9), whereas only a short life-

span of 50 cycles with parasite cycling was achieved, demonstrating the unique ability of the AAS structure for Li metal protection. Furthermore, the effect of Al content in the AAS structure was assessed, by etching the AAS spheres with 0.1 M HCl solution. The morphology of the etched AAS sphere is shown in Fig. S10a, for which a mass ratio of Si: 53.572%, Al: 46.428% was obtained. Consistently, lower specific capacity of lithiation ~ 662 mAh g^{-1} is obtained for the etched AAS (1326.1 mAh g^{-1} for AAS), as shown by the 1st discharge curves (Fig. S10b). The cycling stabilities of Li anodes on the AAS structures with/without etching process are shown in Fig. S10c, whereas better performance belongs to the unmodified AAS, demonstrating the importance of high Al content in the core part of AAS to generate abundant Li_3Al_2 sites for uniform Li nucleation. Also, the Al core is an important backbone material of the AAS. In contrast, another type of Si-Al alloy with Si as dominant element (Si: 92.932%, Al: 7.068% in mass ratio) was studied, whereas poor cycling were obtained whatever the sintering temperatures (Fig. S11).

As a proof-of-concept, the AAS was applied to protect Li anode in Li ‖ $LiFePO_4$ full cells. A one-side AAS coated separator was used by keeping the AAS coating with Li anode, then paired with the $LiFePO_4$ cathodes (~0.5 mAh cm^{-2}) to form the full cell. As shown in Fig. 6c, the cell using the AAS coated separator shows distinctly prolonged life-span up to 645 cycles with a capacity retention of 90.5% and a high CE of 99.2%. In contrast, fast capacity fading to ~36 mAh g^{-1} with an average CE of 95.3% and ~80 mAh g^{-1} with an average CE of 97.7% were observed for the cells using bare separator and Al powders coated separator, respectively. Consistently, sharp increases of polarization and reduced capacity were observed for the cells using bare separator (Fig. 6d) and Al powders coated separator (Fig. 6e), indicating the

accumulated side products and the drying-up of electrolytes. In contrast, stable voltage curves were achieved for the cell using the AAS coated separator (Fig. 6f).

Finally, Li‖ $LiNi_{0.88}Co_{0.09}Al_{0.03}O_2$ (NCA) full cells with a high NCA loading of 5 mAh cm^{-2} were assembled. As shown in Fig. 7a, fast capacity fading occurred in less than 100 cycles for the cell using bare electrolyte, while more stable cycling was maintained over 200 cycles for the cell using AAS coated separator. The charge-discharge curves also demonstrate the alleviated polarization increase upon cycling for the cell using AAS coated separator (Fig. 7b). According to the postmortem SEM analyses, tremendous filament side products were observed on both the separator and Li surfaces from cycled the cell using bare separator (Fig. 7c and 7d). For the cell using AAS coated separator, a relatively intact morphology was maintained for the AAS coating layer on the separator (Fig. 7e), and the protected Li foil exhibited a crack-free surfaces with some granular deposits, possibly arising from the residual AAS powders or side products (Fig. 7f). More importantly, under the protection of the AAS coated separator, the pulverization in depth of the Li foil was mitigated (Fig. S12b), which is a general safety concern during the cycling of routine Li anode (Fig. S12a), leading to fast electrolyte drying-up and higher inflammability of the LMBs. Although the gradual capacity loss of the high loading Li‖NCA full cell using the AAS coated separator still needs to be addressed by further investigation of electrolyte and/or interface optimization, the actual results could demonstrate the possibility to suppress significantly the uncontrolled volume change and pulverization of Li anodes by the protective structure via aggressive Al pulverization strategy.

3. Conclusion

To overcome the dendritic Li deposition and undesired cracks of SEI layers rooted in initial uneven Li nucleation, an artificial structure with enriched Li nucleation sites and robust SEI layer was obtained from the AAS through a facile sintering process of Si-Al alloy. Based on the thermodynamically favored Si diffusion towards the outer surface of the AAS, highly lithiophilic and aggressively pulverized structure could be formed for the lithiated AAS structure with generated Li_3Al_2 and $Li_{12}Si_7$ phases, leading to minimized volume change and Li plating/stripping over-potentials upon cycling. Based on this structure, ultra-low Li nucleation over-potential (~0.7 mV) and high CE of Li plating/striping ~97% over 300 cycles could be achieved in carbonate electrolyte. Besides, the AAS coated separator could extend the life-span of a Li ‖ $LiFePO_4$ cell to 645 cycles with a high CE of 99.2%. This work demonstrates the strategy of aggressive Al pulverization coupled with optimal surface chemistry to achieve stable Li metal anodes for high-energy-density LMBs.

4. Experimental Section

4.1. Material Preparation

The AAS was synthesized in a muffle furnace. Commercial Si-Al alloy powders (Tianjin Metallurgy Technology Co, Ltd) were heated in the furnace under the air atmosphere from room temperature to 1000 ℃ for 3 h by a heating rate of 10 ℃ min^{-1}. After cooling down to room temperature, the AAS powders were obtained by grinding them uniformly in an agate mortar. Al powders (Aladdin Industrial, Inc) were ball-milled before use in a planetary activator (QM-3SP2,

Nanjing NanDa Instrument Plant Co, Ltd) for 14 h in a solution mixture of deionized water and absolute ethyl alcohol (1:1, v/v).

4.2. Electrochemical Measurements

The electrochemical tests were performed using a carbonate electrolyte of 1 M $LiPF_6$ in EC:DEC (1:1, v/v) with vol. 5% FEC. All the electrolyte components were purchased from Sigma-Aldrich Co, LLC. The AAS or Al powders were mixed with Super-P and polyvinylidene fluoride (PVDF, Sigma-Aldrich Co, LLC) in a weight ratio of 7:1:2 in N-methyl-2-pyrrolidone (NMP, Aladdin Industrial, Inc). The as-obtained slurries were casted on Cu foils, followed by vacuum drying at 120 °C for 12 h to form the working electrodes used for Li plating/stripping tests. The same method was applied to obtain the simple SiO_2/Al_2O_3 (Aladdin Industrial, Inc) mixture coated electrodes. For the tests of symmetric cells or Li ‖ $LiFePO_4$ full cells, the AAS or Al powders contained slurries were casted on Celgard separator films (thickness: 20 μm) followed by vacuum drying at 60 °C for 12 h, and the coated layer was kept in contact with Li foil. CR2032 Coin cells were used for assembly in which an electrolyte amount of 50 μL was deposed.

For cycling tests of Li ‖ Cu cells, Li foil was used as counter and reference electrodes, and the AAS or Al powders coated electrodes were used as working electrodes. Li plating was performed at 0.5 mA cm^{-2} for an areal capacity of 1 mAh cm^{-2}, followed by Li stripping up to a cutoff potential to 0.5 V vs. Li/Li^+ using a battery testing system (LandCT2001 from LAND electronics Co, Ltd). The EIS spectra were measured using a potentiostat/galvanostat 1470E equipped with a frequency response analyzer 1455A from Solartron. The EIS measurements

were carried out in the frequency range from 1×10^{-1} to 1×10^{5} Hz with a voltage perturbation of 5 mV.

The $LiFePO_4$ cathodes were obtained by casting the slurry of $LiFePO_4$:Super-P:PVDF (8:1:1, w/w/w) on Al foils, followed by vacuum drying at 120 ℃ for 12 h. The areal loading of $LiFePO_4$ cathodes is ~0.5 mAh cm^{-2} (160 mAh g^{-1} of active $LiFePO_4$ material). The Li ‖ $LiFePO_4$ full cells were pre-cycled for three cycles at charge/discharge rates of 0.1C/0.1C in a voltage window of 2.5-4.4 V vs. Li/Li^+, followed by cycling at 0.5C/0.5C. For Li‖NCA cells, thick NCA electrodes with a high areal capacity loading of ~5 mAh cm^{-2} were provided by CEC New Energy (Wuhan) Research Institute Co., LTD. All the Li‖NCA cells were pre-cycled for six cycles at charge/discharge rates of 0.1C/0.1C in a voltage window of 2.8-4.3 V vs. Li/Li^+, followed by cycling at 0.2C/0.2C.

4.3. Characterizations

The element content of Si-Al alloy powder was detected by an Inductively Coupled Plasma Optical Emission Spectrometer (ICP-OES, SPRECTRO ARCOS II). The particle size analysis was measured by a laser diffraction sensor (HELOS-OASIS). After being cycled, the electrodes were carefully disassembled in an argon-filled glovebox (MBraun, $H_2O \leqslant 0.1$ ppm, $O_2 \leqslant 0.1$ ppm), and rinsed with pure DMC to eliminate the residual trace of solvents and salts, then stored in the glove box for further characterization. The microscopy analysis of the surface morphology was observed using SEM (FEI, QUANTA 250 FEG) and TEM (JOEL 2100, 200kV), and the elemental distribution was examined using energy dispersive X-ray spectroscopy (EDS). The

samples for cross-sectional characterizations were prepared by Focused Ion Beam (FIB, Auriga). Surface chemistry analysis was conducted with a PHI 3056 XPS, which was excited by a Mg-Kα radiation source at a constant power of 100 W (15 kV and 6.67 mA). The large-scale morphology study was carried out using an optical sealed cell coupled with a confocal laser scanning microscope (Zeiss, LSM700). The optical cell was purchased from MTI Corporation. BET surfaces and pore size distribution were obtained through nitrogen gas adsorption measurement performed on an ASAP2020 analyzer from Micromeritics, Inc. The crystalline phase analysis was characterized by XRD with a Bruker D8 advanced diffractometer using Cu Kα (λ = 1.5406 Å) radiation (Bruker axs, D8 Advance) between 20° and 90° at 0.02° step s^{-1}. The cell for in-situ Raman and optical measurements was purchased from MTI Corp. The in-situ optical images were recorded using a Leica DVM6 microscopy. The in-situ μ-Raman spectroscopy was carried out on a Renishaw inVia reflex Raman spectrometer coupled with a battery testing system (LandCT2001 from LAND electronics Co, Ltd). During the in-situ μ-Raman measurements, the Raman spectrometer was at an excitation wavelength of 532 nm from an Nd:YAG (neodymium-doped yttrium aluminum garnet) laser operating at 12 mW. The laser sport was focused at a distance of 10 μm from the studied electrode. Each Raman spectrum was accumulated threefold, whereas an accumulation lasted 10 s.

Acknowledgments

This work was supported by the China Scholarship Council (Grant CSC N°201906340005), the Ningbo Natural Science Foundation (Grant No. 2018A610014), the Ningbo 2025 Project (Grant No. 2018B10060), and the National Key R&D Program of China (Grant No. 2018YFB0905400).

Appendix A. Supporting information

Supplementary data associated with this article can be found in the online version at XXX.

References

1. J. B. Goodenough, Energy Storage Mater. 1 (2015) 158-161.
2. D. Lin, Y. Liu, Y. Cui, Nat. Nanotechnol. 12 (2017) 194-206.
3. D. Wang, W. Zhang, W. Zheng, X. Cui, T. Rojo, Q. Zhang, Adv. Sci. 4 (2017) 1600168.
4. Z. Ren, X. Zhang, M. Liu, J. Zhou, S. Sun, H. He, J. Power Sources 416 (2019) 104-110.
5. X. Cheng, R. Zhang, C. Zhao, Q. Zhang, Chem. Rev. 117 (2017) 10403-10473.
6. Y. Takeda, O. Yamamoto, N. Imanishi, Electrochemistry 84 (2016) 210-218.
7. W. Xu, J. Wang, F. Ding, X. Chen, E. Nasybulin, Y. Zhang, J.G. Zhang, Energy Environ. Sci. 7 (2014) 513-537.
8. S. Li, M. Jiang, Y. Xie, H. Xu, J. Jia, J. Li, Adv. Mater. 30 (2018) 1706375.
9. F. Ding, W. Xu, G. L. Graff, J. Zhang, M. L. Sushko, X. Chen, Y. Shao, M. H. Engelhard, Z. Nie, J. Xiao, X. Liu, P. V. Sushko, J. Liu, J. G. Zhang, J. Am. Chem. Soc. 135 (2013) 4450-4456.
10. Y. Li, G. M. Veith, K. L. Browning, J. Chen, D. K. Hensley, M. P. Paranthaman, S. Dai, X. G. Sun, Nano Energy 40 (2017) 9-19.
11. J. Qian, W. A. Henderson, W. Xu, P. Bhattacharya, M. Engelhard, O. Borodin, J. G. Zhang, Nat. Commun. 6 (2015) 6362.

12. D. Lin, Y. Liu, Z. Liang, H. W. Lee, J. Sun, H. Wang, K. Yan, J. Xie, Y. Cui, Nat. Nanotechnol. 11 (2016) 626-632.
13. C. Jin, O. Sheng, J. Luo, H. Yuan, C. Fang, W. Zhang, H. Huang, Y. Gan, Y. Xia, C. Liang, J. Zhang, X. Tao, Nano Energy 37 (2017) 177-186.
14. Q. Li, S. Zhu, Y. Lu, Adv. Funct. Mater. 27 (2017) 1606422.
15. L. Wang, Q. Wang, W. Jia, S. Chen, P. Gao, J. Li, J. Power Sources 342 (2017) 175-182.
16. T. Foroozan, F. A. Soto, V. Yurkiv, S. Sharifi-Asl, R. Deivanayagam, Z. Huang, R. Rojaee, F. Mashayek, P. B. Balbuena, R. Shahbazian-Yassar, Adv. Funct. Mater. 28 (2018) 1705917.
17. F. Wu, Y.-X. Yuan, X.-B. Cheng, Y. Bai, Y. Li, C. Wu, Q. Zhang, Energy Storage Mater. 15 (2018) 148-170.
18. Y. Yuan, F. Wu, G. Chen, Y. Bai, C. Wu, J. Energy Chem. 37 (2019) 197-203.
19. Y. Yuan, F. Wu, Y. Bai, Y. Li, G. Chen, Z. Wang, C. Wu, Energy Storage Mater. 16 (2019) 411-418.
20. J. Ko, Y. S. Yoon, Thin Solid Films 673 (2019) 119-125.
21. Q. Meng, B. Deng, H. Zhang, B. Wang, W. Zhang, Y. Wen, H. Ming, X. Zhu, Y. Guan, Y. Xiang, M. Li, G. Cao, Y. Yang, H. Peng, H. Zhang, Y. Huang, Energy Storage Mater. 16 (2019) 419-425.
22. R. Zhang, X. R. Chen, X. Chen, X. B. Cheng, X. Q. Zhang, C. Yan, Q. Zhang, Angew. Chemie - Int. Ed. 56 (2017) 7764-7768.
23. W. Tang, X. Yin, Z. Chen, W. Fu, K. P. Loh, G. W. Zheng, Energy Storage Mater. 14 (2018) 289-296.
24. T. Liu, Q. Hu, X. Li, L. Tan, G. Yan, Z. Wang, H. Guo, Y. Liu, Y. Wu, J. Wang, J. Mater. Chem. A 7 (2019) 20911-20918.

25. J. Zhao, G. Zhou, K. Yan, J. Xie, Y. Li, L. Liao, Y. Jin, K. Liu, P. Hsu, J. Wang, H. Cheng, Y. Cui, Nat. Nanotechnol. 12 (2017) 993-999.
26. J. Cho, Y. J. Kim, B. Park, Chem. Mater. 12 (2000) 3788-3791.
27. S. Myung, K. Izumi, S. Komaba, Y. Sun, Chem. Mater. 17 (2005) 3695-3704.
28. Z. Peng, S. Wang, J. Zhou, Y. Jin, Y. Liu, Y. Qin, C. Shen, W. Han, D. Wang, J. Mater. Chem. *A* 4 (2016) 2427-2432.
29. D. R. Poirier, Metall. Mater. Trans. B. 45 (2014) 1345-1354.
30. G. Li, H. Li, Y. Mo, L. Chen, X. Huang, J. Power Sources 104 (2002) 190-194.
31. E. Markevich, G. Salitra, F. Chesneau, M. Schmidt, D. Aurbach, ACS Energy Lett. 2 (2017) 1321-1326.
32. X.-Q. Zhang, X.-B. Cheng, X. Chen, C. Yan, Q. Zhang, Adv. Funct. Mater. 27 (2017) 1605989.
33. G. V Zhuang, G. Chen, J. Shim, X. Song, P. N. Ross, T. J. Richardson, J. Power Sources 134 (2004) 293-297.
34. K. Yan, Z. Lu, H. Lee, F. Xiong, P. Hsu, Y. Li, J. Zhao, S. Chu, Y. Cui, Nat. Energy 1 (2016) 16010.
35. Z. Liang, D. Lin, J. Zhao, Z. Lu, Y. Liu, C. Liu, Y. Lu, H. Wang, K. Yan, X. Tao, Y. Cui, P. Natl. Acad. Sci. USA 113 (2016) 2862-2867.
36. G. Bouteau, A. N. Van-Nhien, M. Sliwa, N. Sergent, J.-C. Lepretre, G. Gachot, I. Sagaidak, F. Sauvage, Sci. Rep. 9 (2019) 135.
37. S.-D. Han, S.-H. Yun, O. Borodin, D. M. Seo, R. D. Sommer, V. G. Young, W. A. Henderson, J. Phys. Chem. C 119 (2015) 8492-8500.

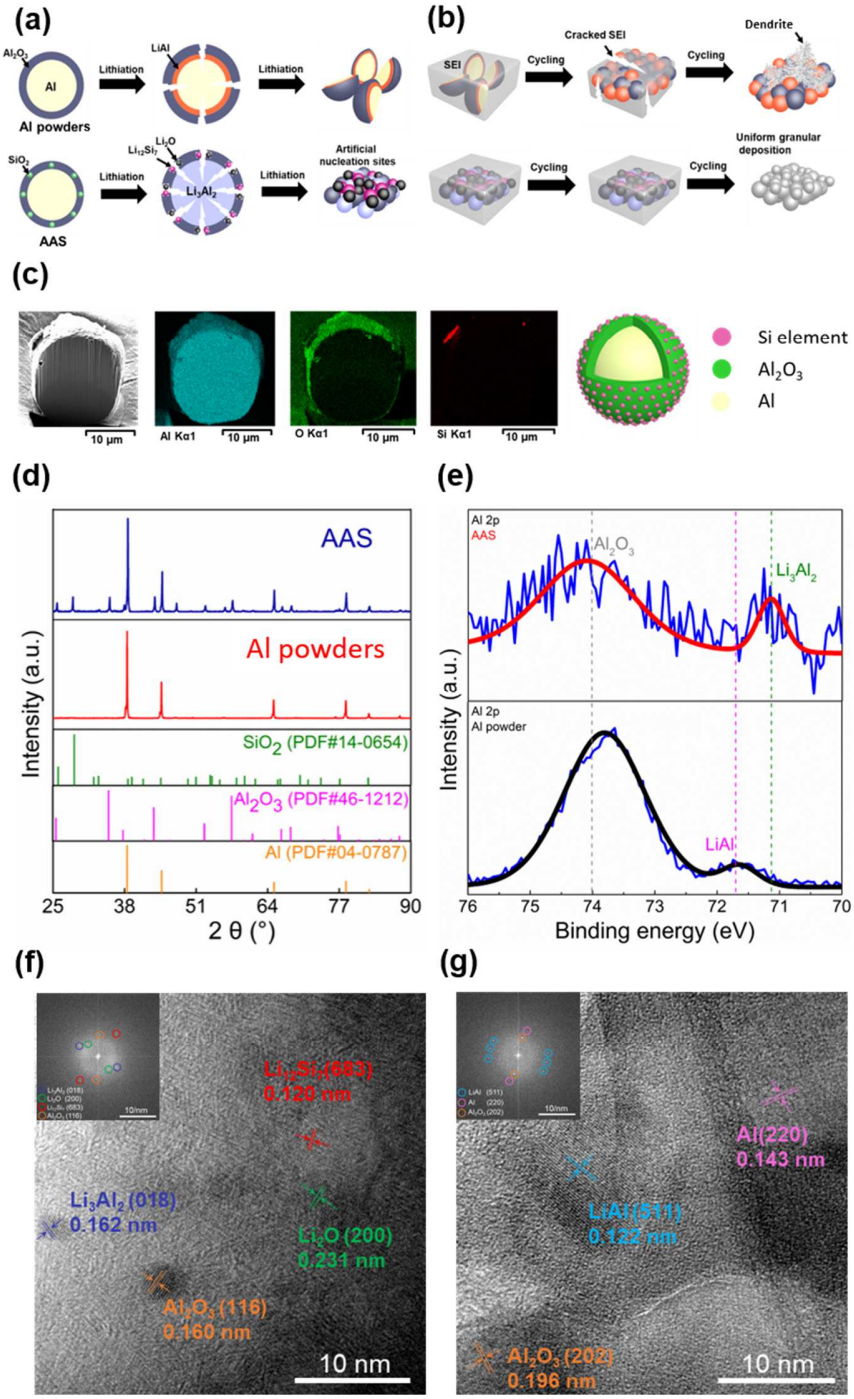

Fig. 1. (a,b) Schematic representations of (a) lithiation and (b) Li plating processes for the AAS and Al powders; (c) Cross-sectional FIB-SEM images and EDS mapping of the AAS; (d) XRD patterns of the AAS and Al powders; (e) XPS Al 2p spectra of the AAS and Al powders reduced to 0 V vs. Li/Li$^+$; (f, g) HRTEM images and FFT patterns of the (f) AAS and (g) Al powders reduced to 0 V vs. Li/Li$^+$.

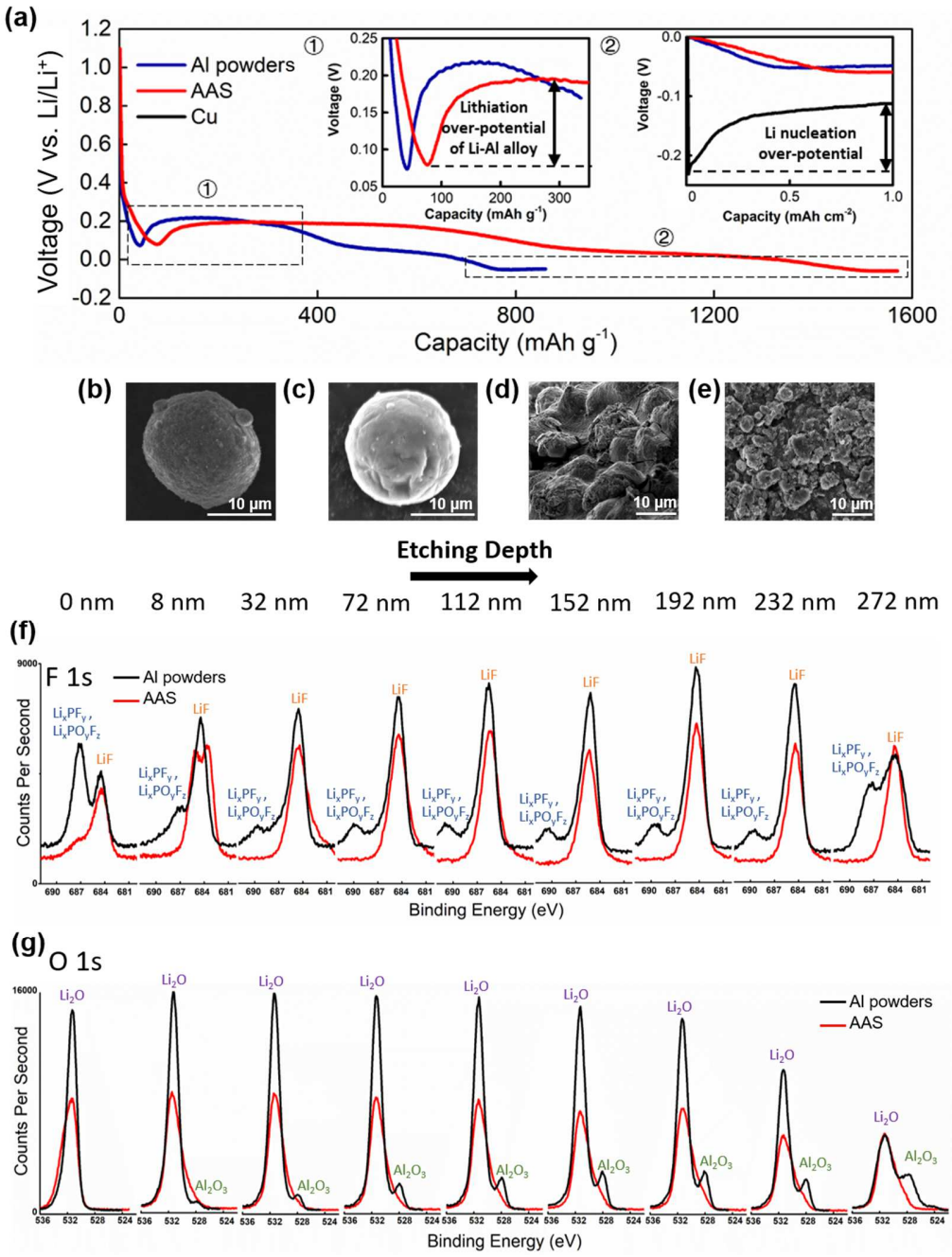

Fig. 2. (a) Discharge curves for the AAS and Al powders lithiated to 0 V vs. Li/Li$^+$, followed by Li plating of 1 mAh cm^{-2}, the curves were recorded at a current density of 0.5 mA cm^{-2}; (b-e) SEM images of the initial (b) Al powder and (c) AAS, lithiated (d) Al powder and (e) AAS; (f, g) XPS analysis of surface components for the cycled AAS and Al powders after 10 cycles, with (f) F 1s and (g) O 1s spectra obtained at different depths during Ar$^+$ sputtering process.

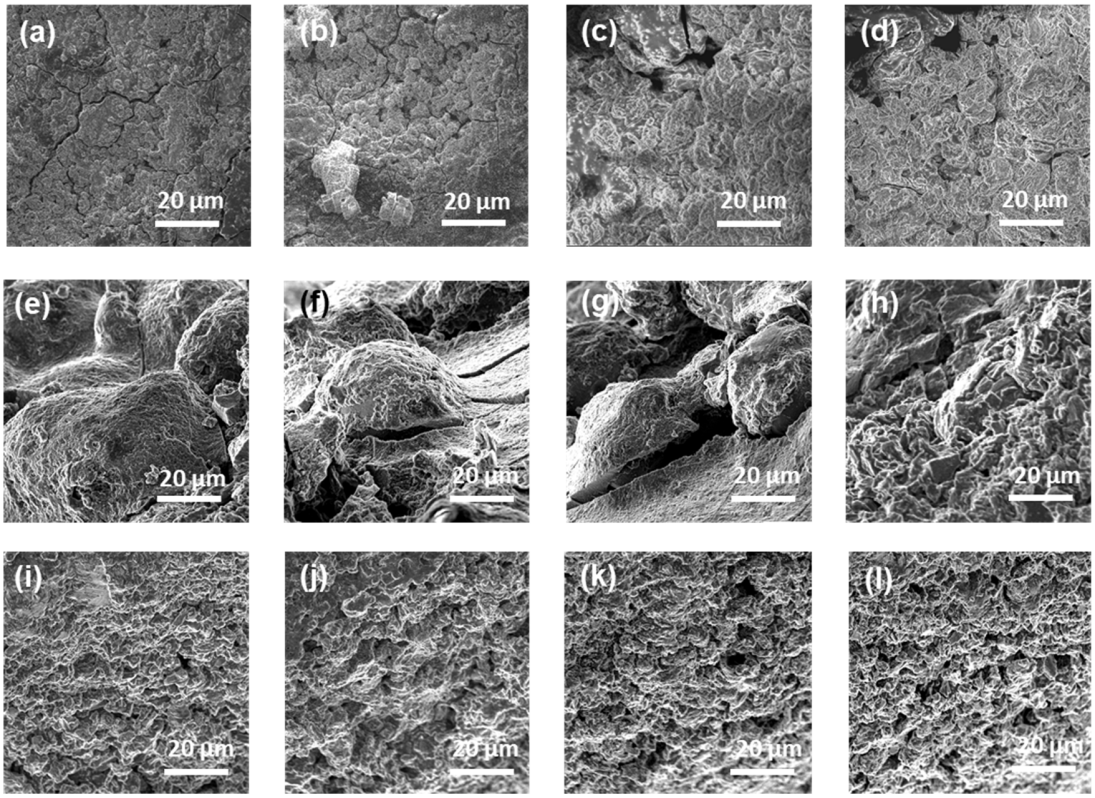

Fig. 3. SEM images of Li plating morphologies on Cu foil at the (a) 1st, (b) 10th, (c) 20th and (d) 50th cycles, on the Al powders at the (e) 1st, (f) 10th, (g) 20th and (h) 50th cycles, on the AAS at the (i) 1st, (j) 10th, (k) 20th and (l) 50th cycle, the cycling was performed at a current density of 0.5 mA cm^{-2} for an areal capacity of 1 mAh cm^{-2}.

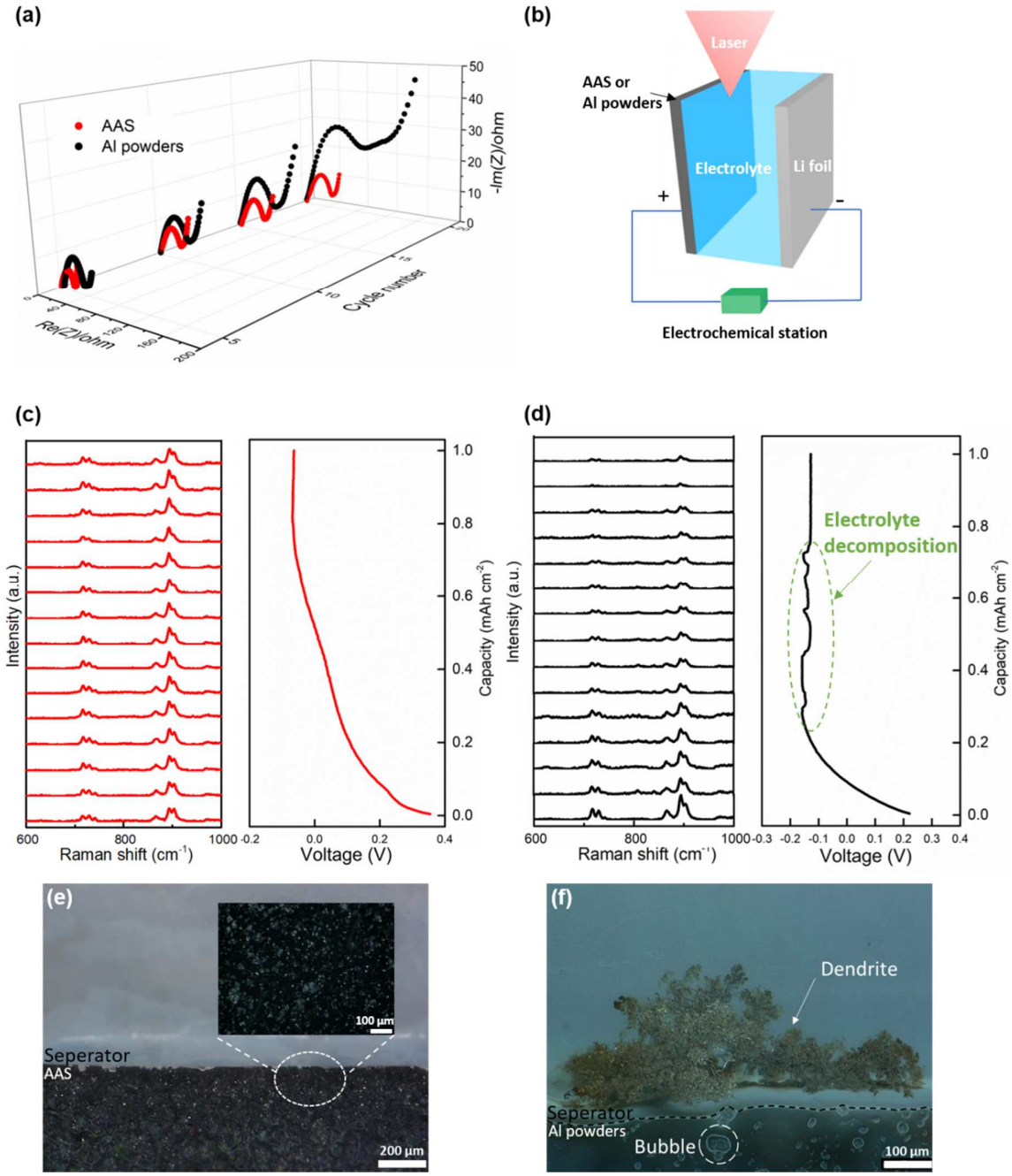

Fig. 4. (a) EIS spectra of the half cells using the AAS and Al powders as working electrodes, at the 5th, 10th, 15th and 20th cycles, at a current density of 0.5 mA cm^{-2} for a fixed areal capacity of 1 mAh cm^{-2}; (b) Schematic representation of the cell for in-situ µ-Raman measurements; (c, d) In-situ µ-Raman spectra and corresponding discharge curves of Li plating on the lithiated (c) AAS and (d) Al powders, at a current density of 0.5 mA cm^{-2} for a fixed areal capacity of 1 mAh cm^{-2}; (e, f) Cross-sectional optical images of 5 mAh cm^{-2} Li plating on the lithiated (e) AAS and (f) Al powders.

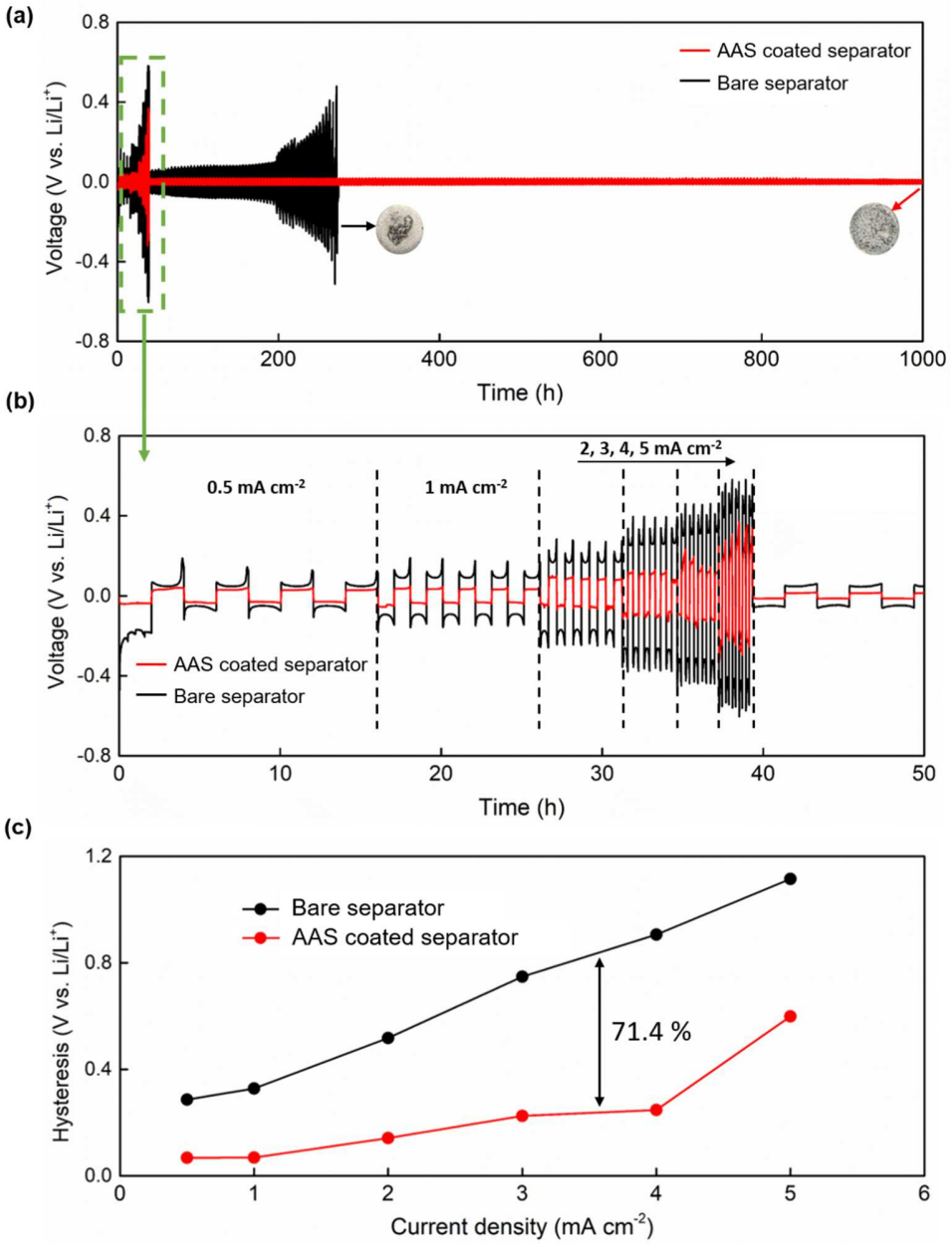

Fig. 5. (a) Galvanostatic cycling performances of symmetric cells using bare separator and the AAS coated separator started with a rate ability test at various current densities of 0.5, 1, 2, 3, 4 and 5 mA cm^{-2}, followed by cycling at a fixed current density of 0.5 mA cm^{-2} with a stripping/plating capacity of 1 mAh cm^{-2}, digital photos of the cycled Li foils are shown beside the related voltage curves; (b) Amplified voltage profiles of the rate capacity test for different current densities in symmetric cells; (c) Cell polarization of the rate ability test for different current densities.

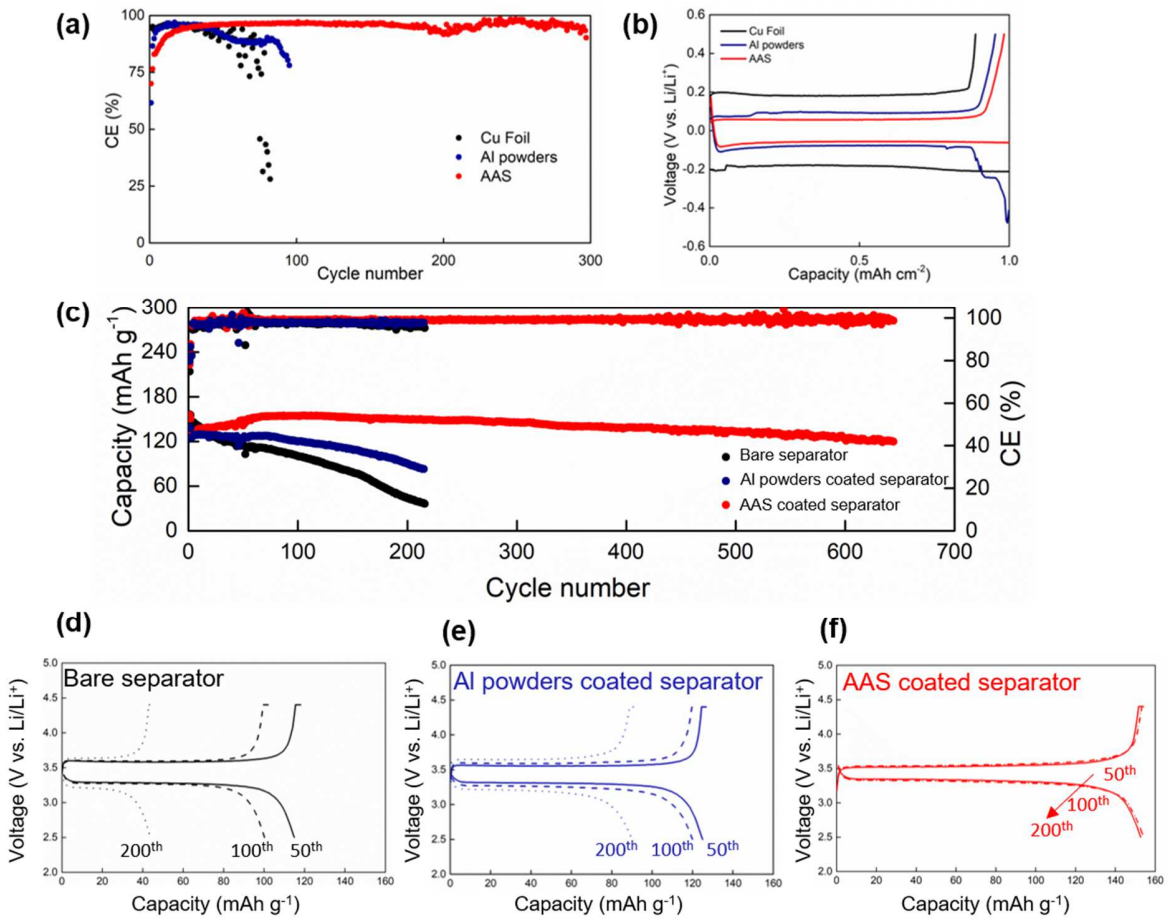

Fig. 6. (a) Li CEs on Cu foil, Al powders, and AAS for Li plating/stripping at a current density of 0.5 mA cm^{-2} for a fixed capacity of 1 mAh cm^{-2}, and (b) their discharge-charge curves at the 50^{th} cycle. (c) Cycling performance of Li ‖ $LiFePO_4$ full cells using bare separator, Al powders and AAS coated separators; (d-f) Charge-discharge curves of the Li ‖ $LiFePO_4$ full cells using (d) bare separator, (e) Al powders and (f) AAS coated separators.

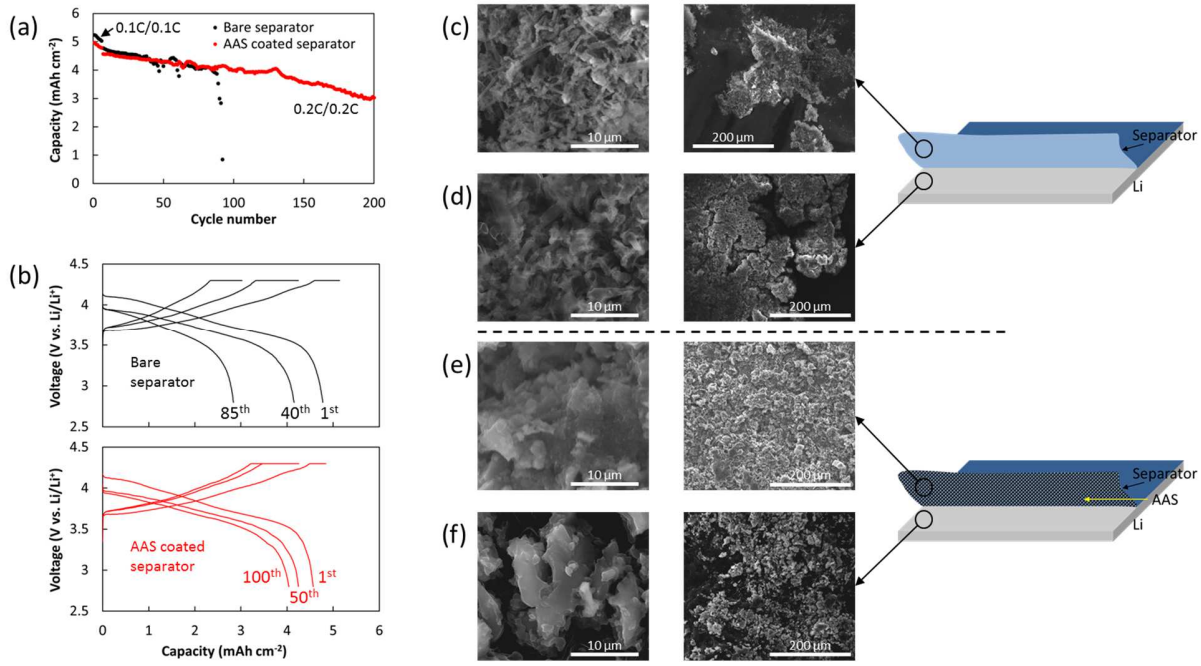

Fig. 7. (a) Cycling performances and (b) Charge-discharge curves of the Li||NCA full cells using bare and AAS coated separators, whereas 1C = 5 mA cm^{-2}; (c-f) Surface morphologies of different components disassembled from the cycled Li||NCA full cells, with (c) bare separator and (d) unprotected Li foil, and (e) AAS coated separator and (f) protected Li foil.

Feihong Ren is currently a Ph.D. candidate at Institut Européen des Membranes (IEM), Université de Montpellier (UM). He received his Master degree in material engineering at University of Science and Technology of China (USTC) in 2019. His research interests focus on lithium metal anodes protection and in-situ μ-Raman spectroscopy on secondary batteries.

Zhendong Li is currently a research assistant at Ningbo Institude of Materials Technology and Engineering (NIMTE), Chinese Academy of Science. He received his B.Sc in chemistry from Xiamen University in 2017. His research interests are focused on electrochemistry and high energy density secondary batteries.

Yun Zhu is currently a M.Sc. candidate at Shanghai University and Ningbo Institute of Materials Technology and Engineering (NIMTE), Chinese Academy of Sciences. He received his B.Sc. in Material Processing and Control Engineering at Nanjing Agricultural University in 2017. His research interests focus on high energy density lithium metal batteries.

Patrice Huguet is professor at the University Montpellier 2 since 2001. In 2000, he joined the European Membrane Institute where he develops new techniques for the characterization of transport processes in ion-exchange membranes. In recent years, his research interest was mainly devoted to the development of original experimental setups, based on confocal Raman microscopy, for measuring water gradients across the polymer membrane working in the fuel cell.

Stefano Deabate joined the European Membrane Institute in 2003 as associate professor (Top School of Engineering Chemistry of Montpellier). His research interests are centered on the investigation of the mass/charge transport mechanisms in condensed matter. His work comprises materials for both electrochemical energy storage (Ni electrode, Li batteries) and production (polymer electrolytes for low temperature fuel cells). The focus of his research is both a better understanding of fundamental issues and the development of novel characterization methods coupling in situ vibrational spectroscopy (IR and Raman) to electrochemical devices.

Dr. Deyu Wang is currently a professor in Ningbo Institute of Materials Technology and Engineering (NIMTE), Chinese Academy of Science. His research is focused on the fundamentals and technologies of the electrochemical energy storage materials & devices, especially on lithium based batteries. He has published ~ 80 papers and filed ~ 40 patents.

Dr. Zhe Peng is currently an associate professor at Ningbo Institute of Materials Technology and Engineering (NIMTE), Chinese Academy of Science. He received his Ph.D. degree from Superior National School of Chemistry of Montpellier, France in 2012. He worked as Alternate Sponsored Fellowship (ASF) of the Pacific Northwest National Laboratory (PNNL) in 2018-2019. His research interests are focused on Electrochemistry and Materials in Lithium secondary batteries.